Monthly Notices
of the
ROYAL ASTRONOMICAL SOCIETY

MNRAS **479,** 111–120 (2018)
Advance Access publication 2018 May 28

doi:10.1093/mnras/sty1392

The first release of the AST3-1 Point Source Catalogue from Dome A, Antarctica

Bin Ma,[1,2,3★] Zhaohui Shang,[1,2,4★] Yi Hu,[1,2] Keliang Hu,[1] Qiang Liu,[1] Michael C. B. Ashley,[5] Xiangqun Cui,[2,6] Fujia Du,[2,6] Dongwei Fan,[1] Longlong Feng,[7] Fang Huang,[8] Bozhong Gu,[2,6] Boliang He,[1] Tuo Ji,[9] Xiaoyan Li,[2,6] Zhengyang Li,[2,6] Huigen Liu,[10] Qiguo Tian,[9] Charling Tao,[11,12] Daxing Wang,[6] Lifan Wang,[2,7,13] Songhu Wang,[14†] Xiaofeng Wang,[12] Peng Wei,[10] Jianghua Wu,[8] Lingzhe Xu,[6] Shihai Yang,[2,6] Ming Yang,[10] Yi Yang,[8,13,15] Ce Yu,[16] Xiangyan Yuan,[2,6] Hongyan Zhou,[9] Hui Zhang,[10] Xueguang Zhang,[7] Yi Zhang,[6] Cheng Zhao,[1,12] Jilin Zhou[10] and Zong-Hong Zhu[8]

Affiliations are listed at the end of the paper

Accepted 2018 May 11. Received 2018 April 28; in original form 2018 March 11

ABSTRACT

The three Antarctic Survey Telescopes (AST3) aim to carry out time-domain imaging survey at Dome A, Antarctica. The first of the three telescopes (AST3-1) was successfully deployed in 2012 January. AST3-1 is a 500 mm aperture modified Schmidt telescope with a 680 mm diameter primary mirror. AST3-1 is equipped with a SDSS *i* filter and a 10k × 10k frame transfer CCD camera, reduced to 5k × 10k by electronic shuttering, resulting in a 4.3 deg^2 field of view. To verify the capability of AST3-1 for a variety of science goals, extensive commissioning was carried out between 2012 March and May. The commissioning included a survey covering 2000 deg^2 as well as the entire Large and Small Magellanic Clouds. Frequent repeated images were made of the centre of the Large Magellanic Cloud, a selected exoplanet transit field, and fields including some Wolf–Rayet stars. Here, we present the data reduction and photometric measurements of the point sources observed by AST3-1. We have achieved a survey depth of 19.3 mag in 60 s exposures with 5 mmag precision in the light curves of bright stars. The facility achieves sub-mmag photometric precision under stable survey conditions, approaching its photon noise limit. These results demonstrate that AST3-1 at Dome A is extraordinarily competitive in time-domain astronomy, including both quick searches for faint transients and the detection of tiny transit signals.

Key words: methods: data analysis – methods: observational – techniques: image processing – techniques: photometric – catalogues – surveys.

1 INTRODUCTION

Small aperture telescopes with wide fields of view (FoVs) have long played a prominent role in time-domain astronomy. Numerous projects have achieved significant success in searching for rare transient events, such as near-Earth asteroids (NEAs), Potentially Hazardous Asteroids (PHAs), supernovae (SNe), gamma-ray bursts (GRBs), and tidal disruption events (TDEs), e.g. PTF (Law et al. 2009) and Pan-STARRS (Kaiser et al. 2002; Chambers et al. 2016). The photometric monitoring of large sky areas also provides very valuable data sets for variability studies of stars and active galactic nuclei.

Bellm (2016) compares the survey capabilities of existing and planned projects, among which telescopes with a diameter less than 1 m are also competitive. The Catalina Real-time Transient Survey (CRTS; Drake et al. 2009) has repeatedly scanned the sky for nearly a decade and detected thousands of SNe. Many areas of astronomy have benefited from such a data set of long-term light curves, e.g. the finding of a possible supermassive black hole binary in a quasar (Graham et al. 2015). The All Sky Automated

★ E-mail: bma@nao.cas.cn; zshang@gmail.com
† 51 Pegasi b Fellow.

Survey for SuperNovae (ASAS-SN; Shappee et al. 2014) deploys telescopes with 14-cm aperture lenses, and has discovered more than 500 bright SNe since 2013, including the most luminous SN candidate ever found (Dong et al. 2016; Godoy-Rivera et al. 2017; however, Leloudas et al. 2016 and Margutti et al. 2017 suggest it is a TDE event). Recently, there has been growing interest to develop transient surveys using 50-cm class telescopes. In Hawaii, the Asteroid Terrestrial-impact Last Alert System (ATLAS; Tonry 2011; Tonry et al. 2018) consists of two 50-cm telescopes with 30 deg^2 FoVs. ATLAS automatically scans the entire accessible sky several times every night. A major science goal of ATLAS is to look for moving objects and provide warnings for killer asteroids. Since its first light in 2015 June, ATLAS has discovered 127 NEAs, 17 PHAs, 9 comets, as well as more than 1000 SNe.[1] Meanwhile in La Silla, Chile, in the Southern hemisphere, blackGEM (Bloemen et al. 2016) is under construction. In Phase 1, it will be an array of three 65-cm telescopes, each with 2.7 deg^2 FoV. In Phase 2, blackGEM is proposed to be extended to 15 identical telescopes. Although ATLAS and blackGEM are equipped with the same CCD cameras, ATLAS has a pixel scale of 1.86 arcsec to maximize its FoV, while blackGEM has a pixel scale of 0.56 arcsec to obtain seeing-limited image quality and to push the survey depth down to $g \sim 22$.

Most ground-based transit surveys utilize small telescopes (aperture sizes around 20 cm) to search for exoplanets. Examples include WASP (Pollacco et al. 2006), HATNET (Bakos et al. 2004), and HATSouth (Bakos et al. 2013). By surveying large areas of the sky to millimag (mmag) precision with rapid cadence, these surveys have discovered a number of exoplanets. Recently, the ongoing Next Generation Transit Survey (NGTS; Chazelas et al. 2012; Wheatley et al. 2018) has employed an array of twelve 20 cm telescopes to find transiting Neptunes and super-Earths.

Near continuous monitoring of the sky enables comprehensive and rapid detections of transient phenomena that are intrinsically variable on short time-scales. Studies of stellar variability also benefit from the long-term continuous photometry that probes a wide range of frequencies. For the highest quality and most continuous data sets, a good site is essential. The Antarctic Plateau has long been known as a premier astronomical site since its atmosphere is extremely cold, dry, tenuous, and stable (Saunders et al. 2009). Thus, it is favourable for optical, infrared, and THz observations. In particular, the decreased high-altitude turbulence above the plateau results in reduced scintillation noise (Kenyon et al. 2006) thereby improving photometric and astrometric performance. The polar night in Antarctica provides the opportunity for continuous observations of up to months, uninterrupted by the diurnal cycle at temperate sites. Moreover, Lawrence et al. (2004) reported a mean seeing of 0.27 arcsec (median 0.23 arcsec) at Dome C above a low boundary layer (Bonner et al. 2010), drawing the attention of astronomers worldwide.

In 2005, the 21st CHInese National Antarctic Research Expedition (CHINARE) arrived at Dome A, the highest location of Antarctic plateau, for the first time. Since then Chinese astronomers have conducted site testing campaigns at Dome A in partnership with international collaborators. The results from various facilities have revealed that Dome A has an atmospheric boundary layer as thin as 14 m (Bonner et al. 2010), a strong temperature inversion above the snow surface but low wind speed (Hu et al. 2014), low water vapour (Shi et al. 2016), low sky brightness, and low cloud fraction (Zou et al. 2010; Yang et al. 2017). In addition to site testing, the first generation telescope, Chinese Small Telescope ARray (CSTAR; Yuan et al. 2008; Zhou et al. 2010), continuously monitored an area of 20 deg^2 centred at the South Celestial Pole for three winters beginning in 2008. The photometric precision from CSTAR reached 4 mmag after various efforts to correct the inhomogeneous effect of clouds (Wang et al. 2012), ghost images (Meng et al. 2013), and diurnal effects (Wang et al. 2014a). CSTAR produced many studies of variable stars and exoplanets (e.g. Wang et al. 2011; Wang et al. 2014b; Wang et al. 2015; Yang et al. 2015; Zong et al. 2015; Liang et al. 2016; Oelkers et al. 2016).

Following CSTAR, the Antarctic Survey Telescopes (AST3) were conceived as the second-generation optical telescopes at Dome A, and designed for multiband wide-field surveys, with each telescope operating with a different fixed filter. The AST3 telescopes would not only have larger apertures than CSTAR but would also have full pointing and tracking functions. The first and the second AST3 – AST3-1 and AST3-2 – were installed at Dome A in 2012 and 2015, respectively, by the 28th and 31st CHINAREs. The third telescope, AST3-3, is under construction and will be equipped with a $K_{\rm dark}$-band near-IR camera (Burton et al. 2016; Li et al. 2016).

Here, we present the first data release (DR1) of photometric products from AST3-1 in 2012. These data have been used for a study of variable stars in one of the fields (Wang et al. 2017). We organize the paper as follows: the telescope and CCD camera are introduced in Section 2, the observations are described in Section 3, the data reduction in Section 4, we present the photometric results in Section 5 and summarize the paper in Section 6.

2 AST3-1

The AST3-1 telescope, built by the Nanjing Institute of Astronomical Optics & Technology (NIAOT), has a modified Schmidt system design (Yuan & Su 2012). It has an entrance pupil diameter of 500 mm, a primary mirror diameter of 680 mm, a focal ratio of *f*/3.73 and a large FoV with a diameter of $\sim 3^\circ$. The main features of AST3-1 include good image quality, a planar focal plane, reduced atmospheric dispersion, an absence of distortion, and a compact structure. In the *r* or *i* bands, 80 per cent of the light energy of a point source is encircled within 1 arcsec. The largest distortion across the FOV is 0.012 per cent, i.e. roughly 1 arcsec across the 3° diameter. The tube is about half the length of a traditional Schmidt telescope. Unlike CSTAR, AST3-1 has full pointing and tracking components, as well as a focusing system. AST3-1 is powered by the PLATeau Observatory for Dome A[2] (PLATO-A; Ashley et al. 2010). As an evolution of the original PLATO, PLATO-A is a self-contained automated platform for supplying power of 1 kW continuously for a year, with internet access provide by Iridium satellites.

AST3-1 is equipped with an SDSS *i* filter and the CCD camera is designed and manufactured by Semiconductor Technology Associates, Inc. The CCD has 10 560 × 10 560 pixels with a pixel size of 9μm, corresponding to 1 arcsec in the focal plane of AST3. To avoid the possible malfunction of a mechanical shutter, frame transfer mode was adopted to terminate the exposure. To do so, the CCD is divided into two parts with equal area: the frame store regions and the exposure area, giving an effective FoV of $2\overset{\circ}{.}93 \times 1\overset{\circ}{.}47$, or ~ 4.3 deg^2. There are 16 individual readout amplifiers to accelerate the readout, which takes 40 s in slow mode (100 kHz), or 2.5 s in fast mode (1.6 MHz). The CCD chip is cooled by a thermoelectric

[1] http://www.fallingstar.com/home.php

[2] http://mcba11.phys.unsw.edu.au/ plato-a

cooler (TEC) and takes advantage of the low ambient air temperature at Dome A, which is about −60°C on average in winter (Hu et al. 2014). Detailed lab tests of the camera have been performed by Ma et al. (2012), including linearity, the photon transfer curve, readout noise, dark current level, and charge transfer efficiency. For example, the readout noise is $11e^-$ in fast mode and is reduced to $4\,e^-$ in slow mode. The camera was equipped with an engineering-grade CCD with many defective pixels and nearly half the area in one of the 16 channels was damaged, resulting in an overall 3 per cent loss in effective FoV.

The hardware and software for the operation, control and data (COD) system were developed by the National Astronomical Observatories, Chinese Academy of Sciences (NAOC; Shang et al. 2012; Hu et al. 2016; Shang et al. in preparation). The highly customized hardware consists of main control, disk array and pipeline computers. Each computer is duplicated to provide redundancy in order to minimize single points of failures. Attention to reliability was essential since the system has to run unattended during the observing season in austral winter. In order to ensure successful observations, we have overcome various technical difficulties encountered specifically in Antarctica. We have developed customized, stable, powerful but low power consumption computers and data storage arrays able to work in the harsh environment. Additionally, the software suite includes an automatic survey control, a scheduler (Liu et al. 2018), a data storage system, a real-time data processing pipeline, and a robust photometry data base system. The processing must be done on-site since the available internet bandwidth, and the data communication costs, prohibited bringing back more than a tiny fraction of the data in real-time.

3 OBSERVATIONS IN 2012 AT DOME A

The first AST3 (AST3-1) was deployed to Dome A, Antarctica by the 28th CHINARE team in 2012 January (Li et al. 2012) and became the largest optical telescope in Antarctica. Installed during the bright sunshine of the polar day, AST3-1 had to wait for operation until mid-March when twilight began. After tests of focusing, pointing and tracking, the telescope began commissioning observations. Unfortunately the telescope stopped working on May 8 due to a malfunction in the power supply system. During the March to May period, two major observing modes – the survey mode and the monitoring mode – were performed to verify the performance of the telescope and CCD camera. In survey mode, the footprint covered roughly 2000 $\deg^2$ with 496 fields. The exposure time of each image was 60 s and in total more than 3000 images were obtained. The images were used as reference templates for searching for SNe and other transients; we refer to this as the SN Survey. The telescope also surveyed 50 fields covering the Large Magellanic Cloud (LMC) and 12 fields covering the Small Magellanic Cloud (SMC). Fig. 1 shows the sky coverage of the survey mode. In a separate 'monitoring mode', each of several fields were monitored for hours. The monitored fields include the centre of LMC, a transit field where the exoplanets OGLE-TR-111b, 113b, and 132b are located, as well as the Wolf–Rayet stars HD 117688, HD 136488, HD 143414, and HD 88500. In addition to the surveys, AST3-1 observed many other targets such as stellar cluster, galaxies, quasars, and follow-ups of SNe and GRBs. Since these observations did not have many repeated exposures of the same fields, we do not include these data here. Observation statistics for the survey and monitoring modes are shown in Table 1 and Table 2, respectively.

AST3-1 was commissioned in unmanned operating mode at one of the most remote sites on the Earth, and with extreme site conditions. Non-negligible instrumental effects needed to be modelled to process the data effectively. The main issue was the irregular point spread function (PSF) resulting from significant tube seeing caused by the heat from the camera and the unstable tracking of AST3-1. As seen in Fig. 2, the full width at half-maximum (FWHM) of the stellar images varied from 2 to 6 arcsec with a median of roughly 4 arcsec. The profiles of stars were elongated when unstable tracking occurred. The elongation, defined as the ratio of semimajor to semiminor axis, had a median of 1.09 but exceeded 1.2 in some cases. There was also a polar misalignment of about 0.°7 due to difficulties such as limited working time, manpower, and resources at Dome A, while performing the installation process during daytime. The pointing accuracy was improved to ∼2 arcmin after TPoint correction[3] was applied to compensate for polar misalignment.

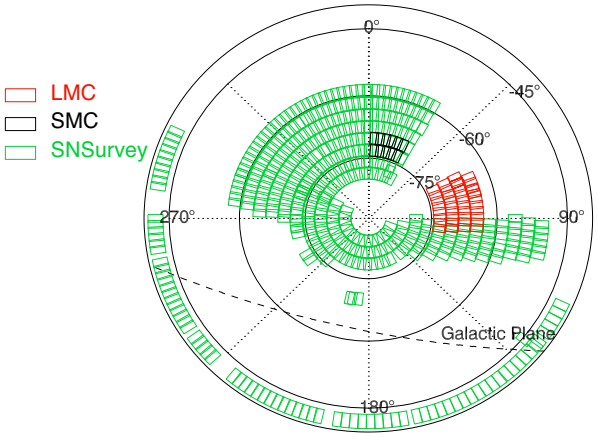

Figure 1. The sky coverage of survey observations from AST3-1 in 2012. The small boxes denote the size and shape of the AST3 FoV while the colours indicate different surveys according to the legend. The dashed line is the Galactic plane.

4 DATA REDUCTION

The raw data from AST3-1 were retrieved by the 29th CHINARE team in 2013. The preliminary reduction of the raw science images involved corrections for CCD cross-talk, over-scan, dark current and flat-fielding. Fig. 3 illustrates an example of the reduction of a raw image in the Transit field. We then performed photometry on the pre-processed images and applied flux and astrometric calibrations on the extracted source catalogues. Light curves were built by cross-matching catalogues in the same field. Each step is detailed in the respective subsection below, particularly for custom methods used to derive the dark current and in constructing the flat-field.

4.1 CCD cross-talk

CCD cross-talk can occur when multiple outputs from the CCD are read out simultaneously. If one amplifier reads a saturated pixel, the pixels that are read simultaneously by the other amplifiers are influenced. This effect appears as ghosts in the image and can be either positive or negative depending on the CCDs. Since there are 16 readout amplifiers in AST3-1's CCD camera, the cross-talk effect is significant. Each saturated star results in 15 negative ghosts in other readout regions and the stars that overlap these ghosts appear

[3] http://www.tpointsw.uk/

Table 1. Statistics of the AST3-1 survey mode observations in 2012.

Object	No. of fields	Sky coverage (deg^2)	No. of frames	Total exposure time (h)	No. of sources detected
LMC	50	200	664	10.60	3038 210
SMC	12	50	55	0.9	227 608
SN Survey	496	2000	3084	51.4	12 768 876

Table 2. Statistics of the AST3-1 monitoring mode observations in 2012.

Object	RA (deg)	Dec. (deg)	No. of frames	Total exposure time (h)	No. of light curves
LMC-centre	80.894	−69.756	4183	58.6	815 589
Transit	163.9	−61.5	3158	35.0	764 279
HD117688	203.3755	−62.317	655	5.0	137 206
HD136488	231.0471	−61.6771	660	4.2	148 798
HD143414	240.9557	−62.6933	1442	7.6	66 284
HD88500	152.633	−60.6451	591	2.2	41 578

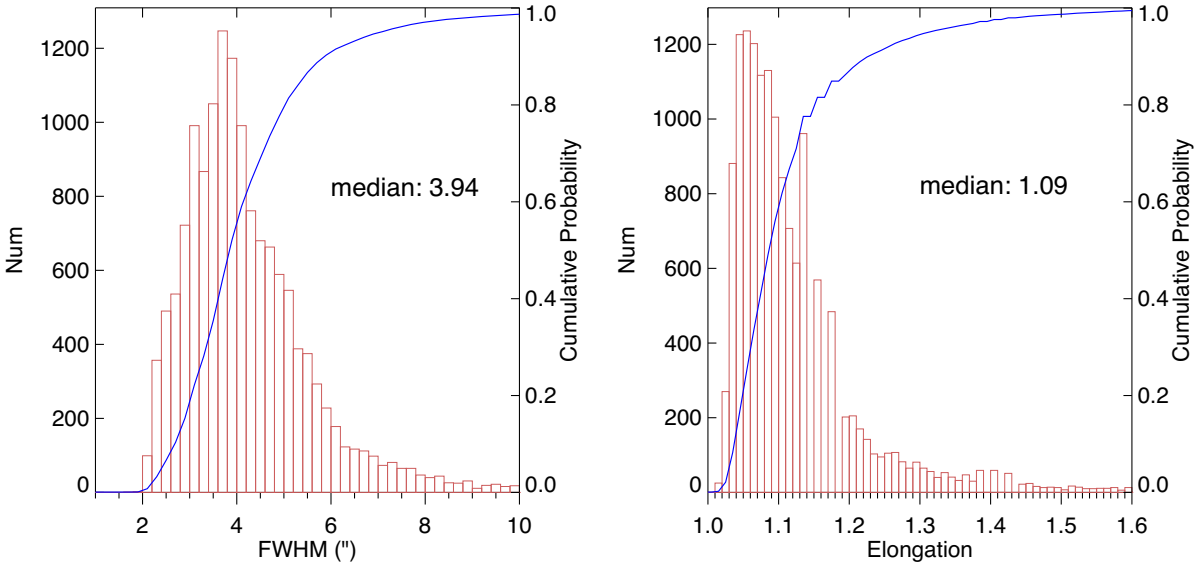

Figure 2. Statistics for the image quality of the AST3-1 2012 commissioning observations. Left-hand panel: FHWM; right-hand panel: elongation.

darkened. To correct for this effect, we compared the values between the ghosts and their surrounding pixels and derived a uniform cross-talk coefficient $CT = 1.3 \times 10^{-3}$. Then, for each readout, we search for every saturated pixel and add $65535 \times CT \sim 85$ ADU to the corresponding pixels at the same physical location in the other 15 readouts.

4.2 Overscan

Since AST3-1's camera has no mechanical shutter, even a 0 s exposure is exposed during the frame transfer period, which takes 434 ms, and consequently cannot be used as a bias frame. Therefore, the median of overscan columns on each readout was subtracted to remove the consequences of any voltage variations.

4.3 Dark current

Dark currents in the AST3-1 camera were significantly high due to the heat dissipation from the CCD, which had a median temperature of −46°C. While the dark current level is less than the sky brightness, the dark current non-uniformity can exceed the photon noise from the sky background. For example, the image a0331.116.fit taken at $t_{CCD} = -40$°C has a median background of 620 ADU. The rms of the background is 55 ADU, which is roughly three times the photon shot noise (19 ADU). Therefore, it is critical to correct the dark current. However, dark frames could not be obtained during the observing season because of the shutterless camera and the unattended site in winter. We developed a simple but effective method to derive the dark current frame from the scientific images (Ma et al. 2014). Here, we briefly describe this method.

The intensity I of a pixel (x, y) can be written as

$$I(x, y) = S + D(T) + \Delta d(T, x, y), \quad (1)$$

where S is the sky background, $D(T)$ is the median dark current level over the entire CCD at temperature T, and $\Delta d(T, x, y)$ is the deviation from the median dark current at pixel (x, y). The stars are ignored because they can be removed by a median algorithm when combining a large number of images from various fields.

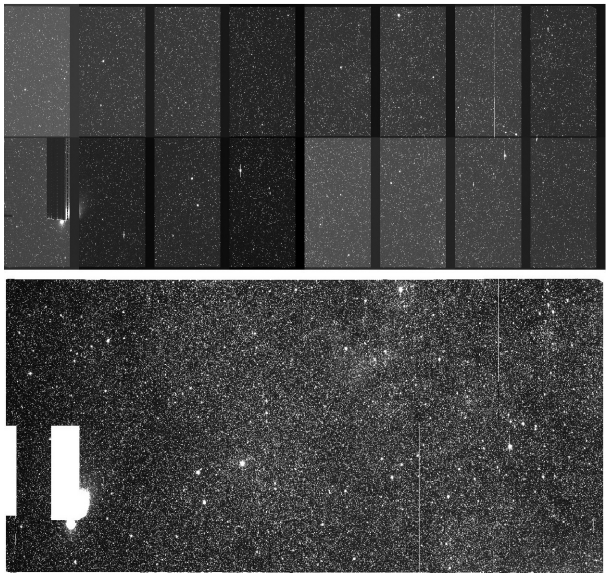

Figure 3. Upper: an example of a raw frame from the Transit field where 16 readouts are obvious due to differing bias levels and overscan. Lower: the pre-processed image from this example; two white regions in the left-lower readout mask the damaged part of CCD.

The sky brightness is adequately flat spatially after twilight (Yang et al. 2017) and therefore is taken as a constant. In equation (1) the sum of the first two position-independent terms S and $D(T)$ is practically the median value of the full image I_0. We denote the later term as a fluctuation term, which describes the temperature and position-dependent effect of dark current. Considering two images taken with the same exposure time and temperature T_0, the sky brightnesses will in general be different. Recall equation (1), the two images have different position-independent terms but the same position-dependent term:

$$I_1(x, y) = I_{0,1} + \Delta d(T, x, y),$$
$$I_2(x, y) = I_{0,2} + \Delta d(T, x, y). \quad (2)$$

Supposing $I_{0,2}$ is brighter, $I_1(x, y)$ can be scaled to the equivalent median level of $I_{0,2}$ by multiplying by the ratio $k \equiv I_{0,2}/I_{0,1}$:

$$I_1'(x, y) = kI_1(x, y) = I_{0,2} + k\Delta d(T, x, y). \quad (3)$$

Subtracting $I_2(x, y)$ from $I_1'(x, y)$ removes the constant term and leaves only the fluctuation term. Consequently the non-uniformity of dark current at temperature T can be calculated from the image pair:

$$\Delta d(T, x, y) = \frac{I_1'(x, y) - I_2(x, y)}{k - 1} = \frac{kI_1(x, y) - I_2(x, y)}{k - 1}. \quad (4)$$

Adding the space-varying term $\Delta d(T, x, y)$ to the median level $D(T)$, we can derive the dark frame at temperature T_0 and exposure time t_0. Before applying the dark correction, the dark frame needs to be scaled to match the temperature and exposure time of the scientific images. However, it is insufficiently accurate to interpolate via the relationship between dark current level and temperature or time. Instead we use the dark current level of warm pixels as the scale parameter – these are high enough for precision determination and have an identical response to temperature and time as normal pixels.

This technique for correcting for dark-current non-uniformity has proved to be sufficiently robust. For the example above, the background rms is reduced to 25 ADU, which pushes the limiting magnitude 1 mag deeper.

4.4 Flat-fielding

We constructed a master flat-field frame by median-combining numerous twilight frames. However, the brightness of the twilight sky is not uniform, and the gradient varies with the Sun elevation and angular distance to the Sun. Therefore, the varying gradients in individual twilight frames will introduce systematic uncertainty in the median-combined frame. We correct for the brightness gradient following the method discussed by Wei et al. (2014).

AST3-1 obtained a total of 2451 twilight frames during its 2012 observations. We selected the images that had adequate sky intensity but were still within the linearity range of the CCD, i.e. between 15 000 and 30 000 ADU. We discarded images taken with CCD temperatures above −40°C, leaving a total of 906 twilight images for further analysis. These frames were then median-combined to generate an initial master flat-field. Each twilight image was then divided by this master flat-field to remove gain variation and vignetting, yielding a relative gradient map to the initial master flat-field. We then fitted each gradient map with a two-dimensional inclined plane $Z = a + bX + cY$. By rejecting images which had a large gradient or large fitting residuals, we obtained the final sample of 200 images. Before recombining them, we removed the gradients by dividing them by their linear fitting plane. This process was repeated for each readout separately rather than for the full frame, since a non-linear gradient variation was observed across the entire frame.

Finally, we combined the gradient-corrected images to obtain the final master flat-field. To compare the quality of the initial and final versions, we constructed the rms image of two samples. The initial rms map showed a four-times increase from the centre to the edge, while the final rms map exhibits a rather uniform value across the entire frame at a level of 0.1 per cent. The accuracy of this flat-field is also confirmed by the photometric results in the next section.

4.5 Photometry and astrometry

SExtractorAperture photometry and astrometry was performed using [4] (Bertin & Arnouts 1996) and SCAMP[5] (Berlin 2006), respectively. We set apertures with radii of 2, 4, 6, and 8 pixel (or arcsec at our plate scale of 1 arcsec pixel^{-1}). As a compromise between bright and faint stars, we adopted the magnitude with an aperture radius of 4 arcsec as the default magnitude. In addition, we derived a Kron-like elliptical aperture magnitude MAG_AUTO, which is usually a robust estimator of total magnitude for galaxies. The windowed position was adopted to calculate the centroid, which has been shown to be as precise as a PSF-fitted position (Becker et al. 2007). To solve for the World Coordinate System, we adopt the Position and Proper Motions eXtended (PPMX, Röser et al. 2008) as the reference catalogue for its small size but high accuracy. The mean source density of PPMX is $\sim 440\,\mathrm{deg}^{-2}$ and its typical one-dimensional scatter is 40 mas. Therefore, with nearly 2000 reference stars with precise coordinates in a typical AST3-1 FoV, we can ensure accurate astrometric calibration. Our observed 1σ astrometric precision is 0.″1 in both RA and Dec., while the internal precision reaches 40 mas for bright stars. This degree of

[4] http://www.astromatic.net/software/sextractor
[5] http://www.astromatic.net/software/scamp

precision with the astrometry is essential for image registration when using difference image analysis (DIA) for transient object detection.

4.6 Flux calibration

We adopted the AAVSO Photometric All-Sky Survey (APASS[6]) DR9 catalogue (Henden et al. 2016) as the reference to calibrate AST3-1's magnitudes. APASS is an all-sky survey conducted in *BVgri* filters. The *i*-band limiting magnitude reaches a depth of ∼16. Compared to the secondary *ugriz* standards (Smith et al. 2002), APASS *i* magnitude has an rms scatter of 0.039 mag and no colour trend (Munari et al. 2014). For the survey fields, we calibrate each frame to APASS. While for each monitored field, we only calibrate the frame with the best image quality to APASS and then adopt this frame as a reference to calibrate the others. The best frame is selected as the one with the most detected sources, which results from a combination of effects such as FWHM, sky brightness, dark current level, and extinction.

When absolutely calibrating an image, we calculate the photometric offsets from instrumental to available APASS *i* magnitudes. The median offset of each frame was used as the zero-point to calibrate the magnitude of all the sources in the frame. The left-hand panel of Fig. 4 presents the offset from an example image (a0420.433.fit). Stars fainter than 14th magnitude exhibit larger dispersions due to the limited depth of APASS. Therefore, we only use 11–14 mag stars to derive the zero-point, which is 0.31 mag with a standard deviation of 0.06 mag in this example. A colour-free zero-point is applied since there was only one filter for AST3-1 in 2012. To investigate the effect of a colour term in the AST3-1 photometric calibration, we also compared the magnitude differences as a function of associated APASS $r-i$ colour, shown in the right-hand panel of Fig. 4(b). The best linear fitting of the magnitude transformation is

$$i_{\rm AST3} = i_{\rm APASS} + 0.3(r-i)_{\rm APASS} + 0.24.$$

Many factors contribute to the difference between two systems, including telescope throughput, CCD quantum efficiency and atmospheric transparency. The low water vapour contents of the atmosphere above Dome A results in significantly better transmission (Sims et al. 2012), which can affect the effective filter curves. The colour coefficient is as large as 0.3. Therefore, caution should be taken when comparing AST3-1's magnitudes with other surveys, especially for extremely blue or red targets. It is also critical when combining magnitudes from multiple facilities to derive the light curve of a colour-varying source. For example, tens of telescopes worldwide contributed to the observations of GW170817, the first optical counterpart of a gravitational wave event (Abbott et al. 2017). However, its $r-i$ colour varied from less than 0 to nearly 1 mag over 4 d. Consequently, large systematic errors of up to 0.3 mag can be induced in the light curve if no colour correction is applied between the various telescopes that are nominally observing in the same band.

In relative calibration for the same field, we find discernible position-dependent variations in magnitude differences between two frames. The reason is probably the variation of FWHM across the CCD and the application of a uniform size of aperture. Fig. 5 illustrates an example of Δ mag between a0410.316.fit and b0409.267.fit, which is the reference image in the field of HD 143414. The magnitude zero-point differs on the order of 0.02 mag across the CCD. To correct for this, we fitted a quadratic zero-point as a function of (X,Y) from using stars with $S/N > 50$, and adopt this to calibrate all the stars. This further reduces the observed scatter in the light curves for bright stars away from the CCD centre compared to a constant zero-point. However, we do not apply the same correction in absolute calibration due to the insufficient accuracy of APASS.

[6]https://www.aavso.org/apass

5 PHOTOMETRIC ACCURACY

In order to estimate the photometric precision of single frame, we compared the magnitude differences between two images and illustrate with an example in Fig. 6. The results are based on two consecutive 60 s images a0330.104.fit and a0330.105.fit with FWHM ∼ 3.7 arcsec. The upper panel shows the differences of aperture magnitude using a 2 arcsec radius and the lower panel shows the 1σ deviation of magnitude difference in each 0.25 mag interval. Overplotted solid lines indicate the photon noise of the signal and the background calculated for various apertures. The photon noise can be written as

$$\sigma = 1.0857\frac{\sqrt{(\pi r^2 S + F)/g}}{F},$$

where r is the aperture radius, S is the sky background, F is the source flux enclosed by the aperture r, and g is the gain of CCD in electrons/ADU. Here, we do not consider the readout noise, which is negligible compared to the photon noise from the sky background. Nor do we include scintillation noise since its level is about 0.1 mmag (Kenyon et al. 2006), much is smaller than the photon noise of the brightest stars. Furthermore, we compare the precisions using aperture radii of 2, 4, 6, and 8 arcsec.

As expected, smaller aperture provides more accurate measurements for the fainter range where the noise is dominated by sky background, while larger aperture is more suitable for bright stars where photon noise from the stars is dominant. For all apertures, the measured noise decreases when brighter and is almost identical to the photon noise in moderate magnitude range. However, it exceeds photon noise for bright stars, tending to be a constant regardless of decreasing photon noise, and starts to rise for stars brighter than $i \sim 11$, which are becoming saturated. The larger the aperture is, the smaller the deviation from photon noise. The constant noise is caused by systematic errors, including instability of the telescope and camera, variation of the atmospheric transparency and seeing, as well as residual errors from the flat-field and dark current corrections. In this example, the best 1σ precisions for four apertures are 10, 1.6, 1.1, and 0.8 mmag, respectively. By comparing with the photon noise it indicates that the systematic error is 10 mmag for aperture of 2 arcsec, but is dramatically reduced to roughly 1 mmag for an aperture of 4 arcsec and is even negligible for aperture of 8 arcsec. Since flux within a radius of 2 arcsec contributes to nearly half of the total flux, the systematic error would be reduced by a factor of 2 at most if little noise comes from annulus beyond 2 arcsec. However, we observe a decrease by a factor greater than 10, which is likely a result of the difficulty in apportioning fluxes to fractional pixels in the 2 arcsec aperture. In summary, the stability of the AST3-1 system is much better than 1 mmag during the 2 min when these two images were taken.

At the faint end when $i > 18.5$, the measured error tends to be flat due to the lack of stars with $\Delta{\rm mag} < 0$ that are detected in one frame, but beyond the detection limit in the other frame. This selection bias results in the measured noise underestimating the real

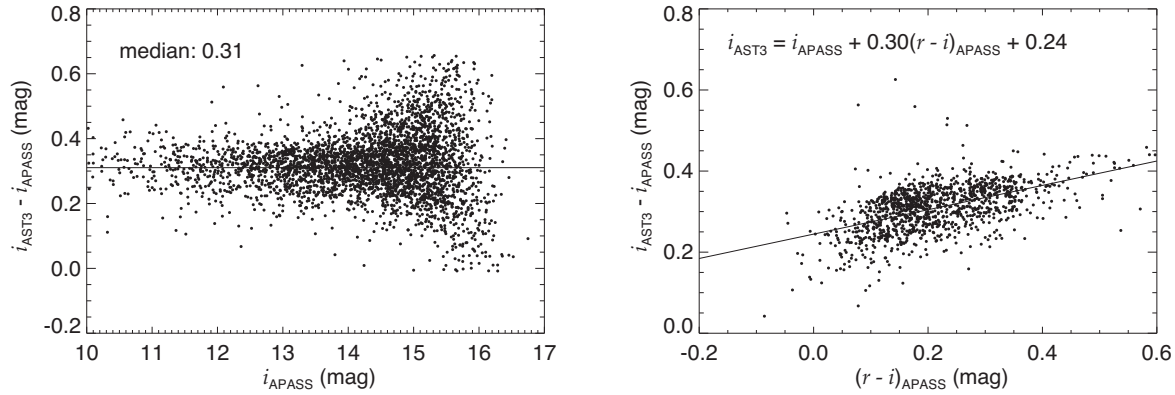

Figure 4. The difference between APASS *i*-magnitudes and AST3-1 instrumental magnitudes of 3636 stars in an example frame a0420.433.fit as a function of (a) the APASS *i*-magnitudes shown in the left-hand panel and (b) the APASS $r - i$ colour for 1207 stars with i_{APASS} between 11 and 14 shown in the right-hand panel. The solid line in the left-hand panel denotes the median value of the magnitude differences, which is adopted as the magnitude zero-point. And the solid line in the right-hand panel is the best linear fit to the colour dependence.

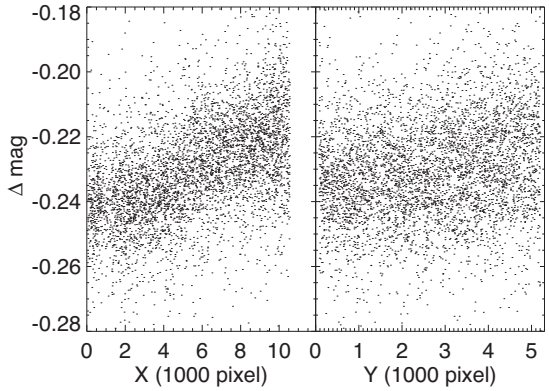

Figure 5. The obvious dependence of Δmag between b0409.267.fit and a0410.316.fit on CCD (X,Y) positions for 4956 stars with $S/N > 50$.

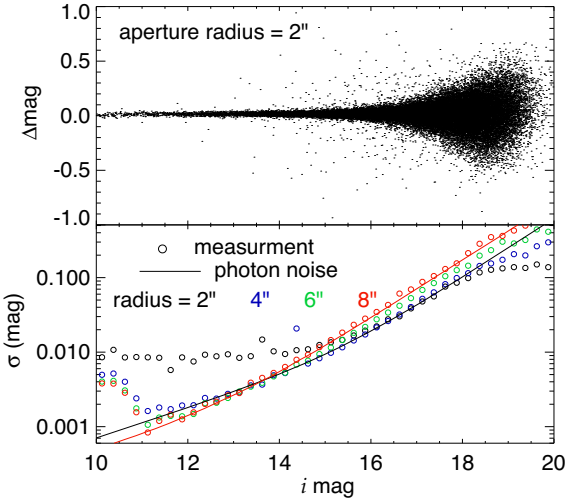

Figure 6. The upper panel presents the magnitude differences between two consecutive 60 s exposures, a0330.104.fit and a0330.105.fit as a function of *i*-band magnitude, measured with a circular aperture of 2 arcsec in radius. The lower panel shows the rms calculated in each 0.2-mag interval and different colours represent the results obtained for different aperture radii. Solid lines indicate the expected error from photon noise for different cases. The performance of the small aperture at the faint end shows a 5σ limiting magnitude of 18.7, while the precision from large apertures at the bright end reaches 0.8 mmag, roughly the photon noise limit. It implies that the systematic error is indiscernible.

noise, so we take the photon noise to define the photometric depth. The $S/N = 5$ limiting magnitude is 18.7 with an aperture radius of 2 arcsec in this case.

These results demonstrate the capabilities of AST3-1 in both detection depth and photometric precision. A deeper detection limit would result from a sharper FWHM and lower sky background. For example, an FWHM of 2.6 arcsec in another image pair, a0331.116.fit and a0331.117.fit with similar sky brightness pushes the 5σ limiting magnitude down to $i \sim 19.3$. Here, we remind the reader that although the seeing at Antarctic sites at a few metres above the boundary layer can be exceptional and reach values of 0.3 arcsec, the surface seeing is quite poor. For instance, the median seeing measured at the ground surface at Dome C is about 2 arcsec (Aristidi et al. 2009). On the other hand, the sky background in these examples is about 19.5 mag arcsec^{-2} and would be one mag darker in a moonless polar night (Zou et al. 2010), which AST3-1 observations did not sample as a result of the power supply problem in early May 2012. Consequently, we infer that AST3 is able to approach a depth of $i \sim 20$ in a 60 s exposure during dark nights under seeing-limited conditions within the turbulent boundary layer.

On the contrary, a sharper FWHM would degrade the photometric precision for bright stars. For example, the precision in an image pair of a0331.116.fit and a0331.117.fit is degraded to 2 mmag. However, FWHM larger than 4 arcsec hardly improves the accuracy, which is usually dominated by systematic errors, but it extends the dynamic range to brighter stars. Therefore, we can optimize the observational strategies for the transit survey mode according to the target magnitude ranges.

For long-term monitoring rather than just two continuous images, the systematic errors become predominant in light curves of bright stars, constraining the detection of tiny variabilities such as exoplanet transit signals. For instance, Fig. 7 shows a diagram of the rms scatters in the light curves versus instrumental magnitude in the field centred on a Wolf–Rayet star HD 143414. This field was monitored on April 8, 9, 10, 11 and May 5, 6 for 1–4 h on each night. We have obtained high-precision photometry with an rms accuracy of ∼5 mmag at the bright end. We also present the theoretical photon-noise limit in a typical observing condition (an integration time of 10 s, an FWHM of 4 arcsec, sky background of 1000 ADU due to full Moon and an extinction of 0.7 mag due to cloud or frost on the mirror). On account of these conditions, photon noise of the brightest stars is 2 mmag. The systematic er-

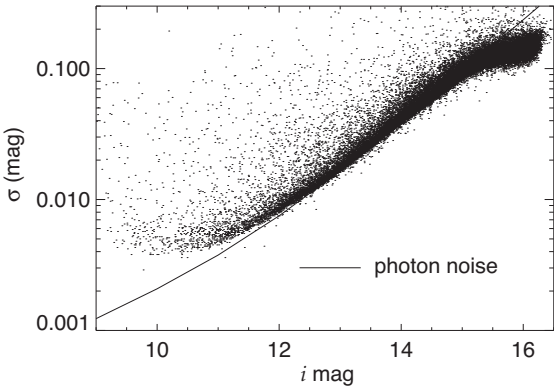

Figure 7. Typical dispersions for AST3-1 *i*-band light curves as a function of stellar brightness in field HD 143414. The solid line shows ideal photon noise under typical observing conditions. The rms uncertainties for bright stars are limited to ∼5 mmag due to systematic errors and relative calibration error.

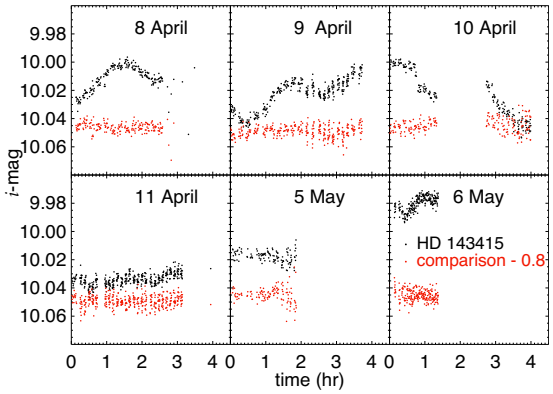

Figure 8. Light curves of one Wolf–Rayet star, HD 143414 (black dots), and a comparison star (red dots) on six days. Time zero denotes the first exposure of the star on each day. The magnitude rms of the comparison star reaches 6 mmag, and HD 143414 exhibits obvious aperiodic variability on time-scale of shorter than an hour.

rors arise from variations in exposure time, FWHM, sky brightness, transparency and position on CCD, as well as errors induced in image corrections and calibrations. The photometric accuracy may be further improved with more careful de-trending by those who are interested in these data. Similar result has been also obtained for the Transit field (see fig. 1 in Wang et al. 2017), while for crowded fields such as the LMC-centre, the photometric accuracy for bright stars is mainly limited by the difficulty of using aperture photometry on blended sources. To improve the precision, PSF photometry is desired and will be performed in the future.

In Fig. 8, we plot example light curves for HD 143414, one of our Wolf–Rayet star targets. The epoch of the observations are labelled. A photometric precision of better than 6 mmag is indicated by the scattering in the light curves of the comparison star, which is 210 arcsec away and ∼0.8 mag fainter. The light curve of HD 143414 exhibits diverse variability on individual days and variabilities shorter than an hour are obvious. Detailed studies of stellar variabilities in the Transit field from the AST3-1 data set can be found in Wang et al. (2017).

Table 3. AST3-1 image Database Schema.

Column Name	Description
Field	Field name
IMAGE	Image name and download link
CATALOGUE	Catalogue name and download link
DATE-OBS	UTC time of the beginning of observation
MJD	Modified Julian date of the beginning of observation
EXPTIME	Integration time (s)
TEMP_CCD	Temperature of the CCD (K)
RA	Right Ascension J2000 of the image centre (deg)
Dec.	Declination J2000 of the image centre (deg)
SKY	Background brightness (ADU)
FWHM	Median full width at half-maximum across the FoV (pixel)
ELONGATION	Median ratio of semi-major to semi-minor axis across the FoV

Table 4. AST3-1 survey Database Schema.

Column Name	Description
ID	Source index
RA	Right Ascension J2000 (deg)
Dec.	Declination J2000 (deg)
MAG	Mean magnitude (mag)
MAGERR	Standard deviation of magnitudes (mag)
COUNT	Number of observations

Finally, we compared the AST3-1 photometry with the Southern Extension of *ugriz* standard stars[7] (Smith et al. 2007). This comparison enables a sanity check of the absolute photometric calibration of AST3-1 observations. The standards are located in a grid of fields spaced roughly every 2 h of RA along Dec. of -30° and -60°, as well as some special fields. Each field with 13.5 arcmin FoV contains dozens of standard stars with high photometric precision. There are six fields observed by AST3-1 in 2012, which are at $\alpha = 0^h$, 2^h, 20^h, 22^h and $\delta = -60^\circ$, as well as the fields of JL 82 and NGC 458. The median magnitude differences between AST3-1 and the standard *i* system in these fields are −0.03, −0.06, −0.01, −0.01, 0.00, and −0.04, respectively. This indicates that the absolute photometric calibration of AST3-1 has an rms of about 0.02 mag. Besides, the $r - i$ colour coefficient in the *i* magnitude transformation is around 0.2 mag.

6 DATA ACCESS

The AST3-1 DR1 data set is available to the community through the Chinese Astronomical Data Center.[8] The data set consists of three parts: AST3-1 images, AST3-1 survey, and AST3-1 light curves.

AST3-1 images includes 14 460 corrected images and corresponding catalogues from both the survey and monitoring observations, accompanied with observation information such as centre coordinates, date, exposure time, and image quality (see Table 3). The AST3-1 survey is a combined catalogue containing more than 16 million sources (see Table 1) down to $i \sim 19$ from the survey observations with positions and magnitudes (see Table 4). The mean

[7] http://www-star.fnal.gov/
[8] http://explore.china-vo.org/

Table 5. AST3-1 light-curve Table Schema.

Column Name	Description
DATE	UTC time of the beginning of observation
MJD	Modified Julian date of the beginning of observation
X	Windowed X position in CCD (pixel)
Y	Windowed Y position in CCD (pixel)
RA	Right Ascension J2000 (deg)
Dec.	Declination J2000 (deg)
FLUX	Flux (ADU)
FLUX_ERR	Flux error (ADU)
MAG_AUTO	Magnitude in Kron aperture (mag)
MAGERR_AUTO	Magnitude error in Kron aperture (mag)
BACKGROUND	Background brightness (ADU)
FWHM	Full width at half-maximum, assuming a Gaussian profile (pixel)
A	Semimajor axis length (pixel)
B	Semiminor axis length (pixel)
THETA	Position angle of semimajor axis (degrees east from north)
FLAGS	SEXTRACTOR flags for the source
R50	Radii enclosing half of total flux
MAG	4 arcsec aperture magnitude (mag)
MAGERR	4 arcsec aperture magnitude error (mag)

values of positions and magnitudes are adopted for the stars detected in multiple images (the median number of observations is three). AST3-1 light curves also contains the sources from the monitored fields, as well as nearly 2 million light curves for the sources with more than 50 detections (see Table 2). Each light curve is presented as a PNG picture and available in multiple formats for download, including FITS binary table, CSV file, and VOTable. Table 5 summarizes the relative information stored in the FITS header. In addition, we provide a tar file for each field containing all light curves in FITS, CSV, and VOTable format, respectively (the link is at the top of the AST3-1 light curves webpage).

7 SUMMARY

In 2012, the first AST3 telescope, AST3-1, was deployed at Dome A in Antarctica to carry out time-domain surveys. During the commissioning phase, AST3-1 surveyed ∼2000 deg^2 fields as well as the LMC and SMC, and monitored a dozen fields including the LMC centre, a field for studying exoplanet transits and some Wolf–Rayet stars. After the raw data were returned to China, we performed aperture photometry, calibrated the magnitudes, and produced light curves in the monitored fields. In this paper, we present the first data release, DR1, of the photometric data from the AST3-1 commissioning surveys. DR1 consists of 14 000 scientific images, 16 million sources bright than $i \sim 19$ with photometry and astrometry, and 2 million light curves.

For faint sources, the 5σ limiting magnitude is $i \sim 18.7$ in 60 s with a typical FWHM of 3.7 arcsec and dramatically deepens to $i \sim 19.3$ with a sharper FWHM of 2.7 arcsec. As a result, we infer a depth of $i \sim 20$ in 60 s during a moonless night with FWHM of 2 arcsec, which is the approximate median ground layer seeing. Along with its wide FoV, AST3-1 is capable of quickly discovering faint transients such as Near-Earth Asteroids, SNe and optical counterparts of GRBs and gravitational wave events. For example, the second AST3 participated in the follow-up of the first electromagnetic counterpart to a gravitational wave signal, GW170817, and detected its quickly fading of luminosity (Hu et al. 2017). At the bright end, ($i \approx 11$), AST3-1 achieved photon noise limited precision of 0.8 mmag, measured from two consecutive 60 s exposures. The AST3-1 photometry in light curves spanning one to two months is stable to a level of 5 mmag, mainly limited by variations in observational conditions and system stability. More careful detrending and binning techniques can further reduce the systematic and statistical uncertainties. Therefore, the data set can be very useful in stellar variability research and the data in some fields are possible to be used for exoplanet detection. Moreover, our results provide suggestions for future strategies, such as choosing the integration time and FWHM for a given magnitude to optimize the precision.

In conclusion, the commissioning of AST3-1 has confirmed its promising prospects in time-domain astronomy, taking advantage of the clear and dark polar night at Dome A. The data set from commissioning is public to the community through the Chinese Astronomical Data Center.

ACKNOWLEDGEMENTS

The authors deeply appreciate the 28th and 29th CHINARE for their great effort in installing/maintaining AST3-1 and PLATO-A. This study has been supported by the National Basic Research Program (973 Program) of China (Grant No. 2013CB834900) and the Chinese Polar Environment Comprehensive Investigation & Assessment Programmes (Grant No. CHINARE2016-02-03), the National Natural Science Foundation of China (NSFC) (Grant Nos. 11403057, 11403048, 11203039, and 11273019). DWF and BLH acknowledge the support from NSFC (Grant No. 11503051), the Joint Research Fund in Astronomy (U1531115, U1731243) under cooperative agreement between the NSFC and Chinese Academy of Sciences (CAS), the National R&D Infrastructure and Facility Development Program of China, 'Earth System Science Data Sharing Platform' and 'Fundamental Science Data Sharing Platform' (DKA2017-12-02-07). Data resources are supported by Chinese Astronomical Data Center (CAsDC) and Chinese Virtual Observatory (China-VO). SW thanks the Heising-Simons Foundation for their generous support. YY acknowledge the support from a Benoziyo Prize Postdoctoral Fellowship. ZHZ acknowledge the support from the 973 Program (Grant No. 2014CB845800), the NSFC (Grants Nos. 11633001 and 11373014), the Strategic Priority Research Program of the CAS (Grant No. XDB23000000), and the Interdiscipline Research Funds of Beijing Normal University.

The construction of the AST3 telescopes was made possible by funds from Tsinghua University, Nanjing University, Beijing Normal University, University of New South Wales, Texas A&M University, the Australian Antarctic Division, and the National Collaborative Research Infrastructure Strategy (NCRIS) of Australia. It has also received funding from the Chinese Academy of Sciences through the Center for Astronomical Mega-Science and National Astronomical Observatories (NAOC). This research was made possible through the use of the AAVSO Photometric All-Sky Survey (APASS), funded by the Robert Martin Ayers Sciences Fund.

REFERENCES

Abbott B. P. et al., 2017, ApJ, 848, L12
Aristidi E. et al., 2009, A&A, 499, 955
Ashley M. C. B., et al., 2010, in McLean I. S., Ramsay S. K., Takami H., eds, Ground-based and Airborne Instrumentation for Astronomy III. SPIE, San Diego, p. 773540

Bakos G., Noyes R. W., Kovács G., Stanek K. Z., Sasselov D. D., Domsa I., 2004, PASP, 116, 266
Bakos G. Á. et al., 2013, PASP, 125, 154
Becker A. C., Silvestri N. M., Owen R. E., Ivezić Ž., Lupton R. H., 2007, PASP, 119, 1462
Bellm E. C., 2016, PASP, 128, 084501
Berlin E., 2006, in Gabriel C., Arviset C., Ponz D., Solano E., eds., Astronomical Data Analysis Software and Systems XV, Vol. 351. Astronomical Society of the Pacific., San Francisco, p. 112
Bertin E., Arnouts S., 1996, A&AS, 117, 393
Bloemen S., et al., 2016, in Hall H. J., Gilmozzi R., Marshall H. K., eds., Proc. SPIE Conf. Ser., Vol. 9906. Ground-based and Airborne Telescopes VI. SPIE, Edinburgh, p. 990664
Bonner C. S. et al., 2010, PASP, 122, 1122
Burton M. G. et al., 2016, PASA, 33, e047
Chambers K. C. et al., 2016, preprint (arXiv:1612.05560)
Chazelas B., et al., 2012, in Stepp L. M., Gilmozzi R., Hall H. J., eds., Proc. SPIE Conf. Ser., Vol. 8444. Ground-based and Airborne Telescopes IV. SPIE, Amsterdam, p. 84440
Dong S. et al., 2016, Science, 351, 257
Drake A. J. et al., 2009, ApJ, 696, 870
Godoy-Rivera D. et al., 2017, MNRAS, 466, 1428
Graham M. J. et al., 2015, Nature, 518, 74
Henden A. A. et al., 2016, VizieR Online Data Catalogue, 2336
Hu L. et al., 2017, Sci. Bull., 62, 1433
Hu Y., Shang Z., Ma B., Hu K., 2016, in Chiozzi G., Guzman J. C., eds., Proc. SPIE Conf. Ser., Vol. 9913. Software and Cyberinfrastructure for Astronomy IV. SPIE, Edinburgh, p. 99130
Hu Y. et al., 2014, PASP, 126, 868
Kaiser N., et al., 2002, in Tyson J. A., Wolff S., eds., Proc. SPIE Conf. Ser., Vol. 4836. Survey and Other Telescope Technologies and Discoveries. SPIE, Waikoloa, p. 154
Kenyon S. L., Lawrence J. S., Ashley M. C. B., Storey J. W. V., Tokovinin A., Fossat E., 2006, PASP, 118, 924
Law N. M. et al., 2009, PASP, 121, 1395
Lawrence J. S., Ashley M. C. B., Tokovinin A., Travouillon T., 2004, Nature, 431, 278
Leloudas G. et al., 2016, Nat. Astron., 1, 0002
Liang E.-S. et al., 2016, AJ, 152, 168
Liu Q., Wei P., Shang Z., Ma B., Hu Y., 2018, Res. Astron. Astrophys., 18, 5
Li Y. et al., 2016, PASA, 33, e008
Li Z., et al., 2012, in Stepp L. M., Gilmozzi R., Hall H. J., eds., Proc. SPIE Conf. Ser., Vol. 8444. Ground-based and Airborne Telescopes IV. SPIE, Amsterdam, p. 84441
Ma B., et al., 2012, in McLean I. S., Ramsay S. K., Takami H., eds., Proc. SPIE Conf. Ser., Ground-based and Airborne Instrumentation for Astronomy IV. SPIE, Amsterdam, p. 84466
Ma B., Shang Z., Hu Y., Liu Q., Wang L., Wei P., 2014, in Holland A. D., Beletic J., eds., Proc. SPIE Conf. Ser., Vol. 9154. High Energy, Optical, and Infrared Detectors for Astronomy VI. SPIE, Montreal, p. 91541
Margutti R. et al., 2017, ApJ, 836, 25
Meng Z. et al., 2013, PASP, 125, 1015
Munari U. et al., 2014, AJ, 148, 81
Oelkers R. J. et al., 2016, AJ, 151, 166
Pollacco D. L. et al., 2006, PASP, 118, 1407
Röser S., Schilbach E., Schwan H., Kharchenko N. V., Piskunov A. E., Scholz R.-D., 2008, A&A, 488, 401
Saunders W. et al., 2009 PASP, 121, 976
Shang Z., et al., 2012, in Peck A. B., Seaman R. L., Comeron F., eds., Proc. SPIE Conf. Ser., Vol. 8448. Observatory Operations: Strategies, Processes, and Systems IV. SPIE, Amsterdam, p. 844826
Shappee B. J. et al., 2014, ApJ, 788, 48
Shi S.-C. et al., 2016, Nat. Astron., 1, 0001
Sims G. et al., 2012, PASP, 911, 74
Smith J. A. et al., 2002, AJ, 123, 2121
Smith J. A. et al., 2007, in Sterken C., ed., ASP Conf. Ser. Vol. 364, The Future of Photometric, Spectrophotometric and Polarimetric Standardization. Astron. Soc. Pac., San Francisco, p. 91
Tonry J. L., 2011, PASP, 123, 58
Tonry J. L. et al., 2018, PASP, 130, 064505
Wang L. et al., 2011, AJ, 142, 155
Wang L. et al., 2017, AJ, 153, 104
Wang S.-H. et al., 2014a, Res. Astron. Astrophys., 14, 345
Wang S. et al., 2012, PASP, 124, 1167
Wang S. et al., 2014b, ApJS, 211, 26
Wang S. et al., 2015, ApJS, 218, 20
Wei P., Shang Z., Ma B., Zhao C., Hu Y., Liu Q., 2014, in Peck A. B., Benn C. R., Seaman R. L., eds., Proc. SPIE Conf. Ser., Vol. 9149. Observatory Operations: Strategies, Processes, and Systems V. SPIE. Montreal, p. 91492
Wheatley P. J. et al., 2018, MNRAS, 475, 4476
Yang M. et al., 2015, ApJS, 217, 28
Yang Y. et al., 2017, AJ, 154, 6
Yuan X., et al., 2008, in Stepp L. M., Gilmozzi R., eds., SPIE Conf. Ser., Vol. 7012. Ground-based and Airborne Telescopes II. SPIE. Marseille, p. 70124
Yuan X., Su D.-q., 2012, MNRAS, 424, 23
Zhou X. et al., 2010, Res. Astron. Astrophys., 10, 279
Zong W. et al., 2015, AJ, 149, 84
Zou H. et al., 2010, AJ, 140, 602

[1]*National Astronomical Observatories, Chinese Academy of Sciences, Beijing 100101, China*
[2]*Chinese Center for Antarctic Astronomy, Nanjing 210008, China*
[3]*School of Astronomy and Space Science, University of Chinese Academy of Sciences, Beijing 100049, China*
[4]*Tianjin Astrophysics Center, Tianjin Normal University, Tianjin 300387, China*
[5]*School of Physics, University of New South Wales, NSW 2052, Australia*
[6]*Nanjing Institute of Astronomical Optics and Technology, Nanjing 210042, China*
[7]*Purple Mountain Observatory, Nanjing 210008, China*
[8]*Department of Astronomy, Beijing Normal University, Beijing 100875, China*
[9]*Polar Research Institute of China, 451 Jinqiao Rd, Shanghai 200136, China*
[10]*School of Astronomy and Space Science, Key Laboratory of Modern Astronomy and Astrophysics in Ministry of Education, Nanjing University, Nanjing 210093, China*
[11]*CPPM, Aix Marseille Univ., CNRS/IN2P3, Marseille 13288, France*
[12]*Physics Department and Tsinghua Center for Astrophysics (THCA), Tsinghua University, Beijing 100084, China*
[13]*Department of Physics and Astronomy, George P. and Cynthia Woods Mitchell Institute for Fundamental Physics and Astronomy, Texas A & M University, 4242 TAMU, College Station, TX 77843, USA*
[14]*Department of Astronomy, Yale University, New Haven, CT 06511, USA*
[15]*Department of Particle Physics and Astrophysics, Weizmann Institute of Science, Rehovot 76100, Israel*
[16]*School of Computer Science and Technology, Tianjin University, Tianjin 300072, China*

This paper has been typeset from a TEX/LATEX file prepared by the author.